Titre: Title:	OpenFiberSeg : open-source segmentation of individual fibers and porosity in tomographic scans of additively manufactured short fiber reinforced composites
Auteurs: Authors:	Facundo Sosa-Rey, Yahya Abderrafai, Audrey Diouf Lewis, Daniel Therriault, Nicola Piccirelli, & Martin Lévesque
Date:	2022
Type:	Article de revue / Article
Référence: Citation:	Sosa-Rey, F., Abderrafai, Y., Diouf Lewis, A., Therriault, D., Piccirelli, N., & Lévesque, M. (2022). OpenFiberSeg : open-source segmentation of individual fibers and porosity in tomographic scans of additively manufactured short fiber reinforced composites. Composites Science and Technology, 226, 109497 (13 pages). https://doi.org/10.1016/j.compscitech.2022.109497

OpenFiberSeg: open-source segmentation of individual fibers and porosity in tomographic scans of additively manufactured short fiber reinforced composites★

Facundo Sosa-Rey[a,*], Yahya Abderrafai[a], Audrey Diouf Lewis[a], Daniel Therriault[a], Nicola Piccirelli[b] and Martin Lévesque[a,**]

[a]Laboratory for Multiscale Mechanics, Polytechnique Montréal, Montreal, H3C3A7, Canada
[b]Safran Composites, A Technology Platform of Safran Tech, Itteville, 91760, France

ARTICLE INFO

Keywords:
Polymer-matrix composites (PMCs)
Porosity/Voids
Short-fibre composites
X-ray computed tomography
3-D Printing

ABSTRACT

From a modelling standpoint, the morphology of additively manufactured (AM) high-performance short fiber reinforced polymer (SFRP) are essential to characterize, yet this task poses great challenges. The method presented extracts individual fibers from tomographic scans and produces a segmentation that is 93.1% precise on average on a per-fiber basis across a large range of fiber filling ratios (5-40 wt.%), needs minimal human input and is scalable to full-sized datasets containing ~10^5 individual fibers. In addition, this tool allows the analysis of the correlated length and orientation distribution of fibers, and the quantification of shear-induced alignment and fiber breakage. The method is validated by successfully reproducing the segmentation of (continuous) fiber reinforced composites published in 2 separate studies and by predicting the fiber volume fraction and material density directly from the tomographic data of SFRPs. The output can serve as a basis for constituent-level mechanical modelling, and to gain insight into the relationship between processing parameters, morphology and mechanical behavior of SFRP. The full source code and imaging data are attached to this publication.

1. Background

Fused Filament Fabrication (FFF) is an additive manufacturing (AM) method in which parts of arbitrary geometry are built layer-by-layer. The use of materials like polyether-ether ketone (PEEK) in FFF is a very active area of research as its mechanical properties similar to human bone, its chemical and thermal resistance, biocompatibility and transparency to medical imaging methods make it a choice candidate for medical implants and prostheses [1–5]. When PEEK is used as a short fiber reinforced polymer (SFRP), the reinforcements can be oriented purposefully, enabling the engineering of parts with high weight-specific material properties [6–8]. As such, reinforced PEEK parts made by FFF are being investigated as possible replacement for heavier metallic components in the automotive and aerospace industry [5, 7–9]. However, several technical challenges complicate the printing process with this material and cause it to under-perform when compared to aircraft-grade aluminum parts [10, 11]. PEEK resin being semi-crystalline with a high melting point, significant shrinkage occurs during solidification, both of thermal origin and due to density and viscosity changes during crystallization [4, 5, 7, 8, 12]. When used in FFF, process parameters, part

★This document is the results of the research project funded by the Canadian National Science and Engineering Research Council.
*Corresponding author
**Principal corresponding author
facundo.sosa-rey@polymtl.ca (Facundo Sosa-Rey); martin.levesque@polymtl.ca (Martin Lévesque)
ORCID(s): 0000-0003-1140-0635 (Facundo Sosa-Rey)

geometry and local cooling history can interact to cause warpage of such severity as to cause print failure [8]. Adding reinforcements can reduce warpage [10] and improve mechanical properties like strength and stiffness [12], but have complex effects on crystallization [12], interlayer bonding and flow dynamics[8]. During extrusion, fibers alignment and flow characteristics are mutually dependent, and in turn affect the bonding dynamics, as fibers present at the bead surface modify diffusion conditions and surface tension [8]. Improper bonding between layers is one of the main causes why FFF parts exhibit inferior mechanical properties to molded parts, most notably across the layers [5, 12]. Porosity is another important factor, introduced both during filament production and by air trapping between passes and layers at deposition [5, 12, 13]. This reduces the effective cross-section of the parts, changes flexural properties through pore collapse, and adversely affects strength since pores act as stress concentration sites [8, 13, 14]. The inclusion of fibers has been shown to be accompanied by increased porosity [6, 9, 12, 15], measured at 20 vol.% for PEEK with 30 wt.% carbon fibers (CFs) [16]. These combined effects makes mechanical modelling of real parts a yet-unsolved challenge [8, 17–22], as all these phenomena need to be considered in concert [8]. To help address this issue, microstructural analysis methods must be developed to enable the extraction of relevant properties from imaging data, particularly at the constituent scale (single fiber and pore).

1.1. Microstructural features

In order to serve as a basis for mechanical behavior prediction, the microstructural analysis must extract the main features affecting stiffness and strength of SFRP materials (other than the inherent properties of the matrix and fibers). Those features have been identified as: the distributions of fiber lengths and orientation [23–28], the uniformity of fibers' spatial dispersion [6, 29], as well as the presence and morphology of porosity and other defects [29–32]. Unlike for the case of continuous fibers, in SFRP those properties are all affected by the processing parameters (both in injection molding or FFF) [6, 17, 25, 26, 28, 33], and are therefore crucial to understand the properties of the parts produced. For instance, shear-induced alignment of fibers and fiber breakage during the different processing steps have decisive impact on the mechanical performance of SFRP parts [6, 8].

Recent advances have been made on constituent-level characterization of SFRP used in FFF, for instance in basalt fiber reinforced polylactic acid (PLA) [34], and CF reinforced PEEK [16]. In both cases, proprietary software was used to perform the critical segmentation steps. Yu et al. [34] do differentiate individual fibers, but in a context of little porosity in the feedstock material (so-called inner-voids, of at most 4.2 vol.%), and moderate infill (up to 20 wt.%). As for CF reinforced PEEK, Sommacal et al. [16] centered their study on porosity distribution, and identified the volume occupied by reinforcements generally, not individual fibers.

In this work, we propose a method of automated constituent extraction from imaging data, called OpenFiberSeg. We draw on existing methods and techniques, complementing and adapting them to the specific case of FFF of reinforced

PEEK. The presence of significant porosity (~20 vol.%), low contrast in the input data and high filling ratios under consideration (up to 40 wt.%) make for a problem that is uniquely challenging. Once this problem is solved, the solution can be applied to a host of fiber reinforced materials, of equivalent or lesser degree of complexity. The intent of open distribution of both source code and imaging data guided the development of this tool, to help accelerate progress in the field.

2. Literature review

X-ray tomography provides volumetric renderings of the microstructure of these solids. However, since CFs and polymeric matrices have similiar densities and elemental composition, the imaging data is low contrast and has considerable noise amplitude [35, 36]. As imaging apparatus are limited to a voxel size of 0.7 to 0.4 μm, fiber identification must be performed on at best a handful of voxels, as they typically have a diameter ranging from 5 to 10 μm. Manual labelling by an expert is possible, but is a tedious, time-consuming task, and subject to inter and intra-observer variability [37]. Automatic segmentation tools are therefore required. Various groups have produced such tools for fiber-reinforced composites, the majority of which consider only two-phase materials (the phases being matrix and reinforcements) [23, 38–41]. When dealing with a third phase (the porosity), the segmentation task considered to be much harder [42, 43], especially when the grayscale values from different phases can overlap each other [43, 44] as they do in FFF reinforced PEEK. In [45], 3-phase segmentation (matrix, fibers and voids) is performed by using a stochastic optimization procedure adapted from [46, 47] to segment small regions of data, and training a neural network with the output. The authors avoid the task of manually labelling training data or the computationally prohibitive task of using the stochastic procedure on full-sized dataset. Their method performs well on real data from glass fiber reinforced polypropylene containing voids, though only visual validation is presented. Using synthetic data with no porosity, they report a per-fiber detection precision of 87.0% (651/748 fibers detected).

If orientation characterisation is the only concern, one traditional method is to use scanning electron microscope images of polished specimen, and determine fiber orientations based on the minor and major axes of the ellipses made by their cross-sections on the specimen surface [48]. However, this method is limited to surface level, is time-consuming, and cannot distinguish between the two orientations that produce the same elliptical cross section [36, 49]. A more modern method based on 3D imaging is to compute the local orientation tensor by obtaining the local structure tensor for neighboring voxels via the Hessian matrix [24, 40, 49]. While being very general and not requiring fiber separation, this method can produce length information only for very highly resolved scans, and it is quite susceptible to noise [50] (though it can be adapted to process poorly resolved scans [39]). Furthermore, the accuracy of the orientation tensor method drops significantly if the gray intensity profile is not Gaussian inside fibers, or for high filling ratios, where fiber contact is more common [23, 24].

2.1. Fiber separation and tracking

To extract richer data pertaining to *individual* fibers, a necessary first step is the segmentation (labelling) of voxels belonging to fibers rather than other phases (matrix, pores, etc). Methods to perform this task include: grayscale value thresholding (Otsu's method) [38] , pattern matching [51, 52], supervised machine learning (for instance K-means clustering used by Qim at DTU [53–55], or deep learning methods like those implemented in commercial software like Dragonfly™[35, 44, 50] or others. One common limitation for all these methods is that for high filling ratios, many fibers will be in close proximity, and their boundary blurred, leaving many missed detections or failing to separate distinct fibers [38, 40]. Since computer vision tools and methods are overwhelmingly aimed at 2 dimensional (2D) images, all of the cited methods are 2D-based. Many missed or false detections could be avoided by taking advantage of the 3 dimensional (3D) nature of tomographic data, but only some efforts have been made towards this goal, for instance using convolutional neural network in 3D [56, 57].

Extracting individual fibers from the voxel-wise label requires a 3D tracking procedure. A fiber tracking method proposed by Whitacre [58] (companion study of Czabaj [51]), uses template matching as the first segmentation step, then the Global Nearest Neighbor algorithm combined with the Kalman filter to estimate fiber trajectories as they are being constructed. This method also incorporates smoothing, track stitching, and a constraint by which fiber trajectories are only accepted if no volumetric overlap occurs in their paths. Whitacre reports 99.4% accuracy of track assignment, but as is pointed out, this is for a relatively small specimen (629 fibers) of *unidirectional* composite, with high scan quality. The authors recognize that for more complex, larger specimen, this method would "increase the computational cost dramatically" [51] (though mainly for the meshing and mechanical simulation than tracking *per se*). The segmentation procedure itself took 2h for 629 fibers on a desktop workstation, while 1 mm^3 of SFRP can contain up to $\sim 10^5$ individual fibers [38]. Assuming linear scaling, that would translates into nearly two weeks' time.

Another tracking method applied to injected glass fiber SFRP was developed by Agyei and Sangid [38] by which the image quality of the scans are first sharpened, then voxels probably containing fibers are flagged using Otsu's method, and clustered using an iterative watershed algorithm. Ellipsoids are fitted to each cluster, and they are connected across 3D space on the basis of the proximity of their centroids. Post-processing ensures that the remaining fibers have tortuosity below a prescribed threshold. Their method successfully tracks 91 682 fibers with a processing time of 55 hrs on a desktop workstation. However, they selected injection-molded glass fiber reinforced polypropylene because of the higher contrast of glass fibers, and there is no porosity to speak of in their samples.

Partially reconstructed fibers have been stitched in different ways. Altendorf selects stitching candidates on the basis of endpoint distance, the angle between the segments, and the angle between segments and the added connecting line [59]. Creveling implement a method by which fiber tracks all considered for stitching, and the most likely candidates which pass a series of checks are selected, including endpoint distance, potential interference with existing tracks, and other tests [52].

In FFF SFRP, the regions surrounding pores are of particular concern from a tracking standpoint. Artifacts at pore boundaries cause many missed and false detections of fibers (even for manual labelling). Hence, a heuristic that overcomes this difficulty need be more complex than those in tracking tools previously published, focused on materials with negligible porosity.

The ultimate objective being mechanical property inference, it is more important that the reconstructed volume be statistically equivalent to the actual solid, rather than any single fiber being found or not. As long as the proportion of phases present is correct, as well as the lengths and orientation distribution of fibers, the extracted microstructure will serve as a representative volume element [60, 61]. This guiding principle will be useful for selecting empirical parameters for aspects of our method that are probabilistic in nature, most notably the stitching partially tracked fibers.

3. Methods

In this work, contrasts in imaging data are first enhanced by histogram equalization. Then 2D-image based pre-segmentation of porosity and specimen boundary (perimeter) is performed with a combination of classical image processing (Otsu's method and Canny edge detection) and fiber regions are located with the use of a machine learning (ML) tool called InSegt [62]. From this voxel-wise labelling, a 3D-based feature extraction is performed: fiber segments are identified by locating centroids and connecting them by the K-nearest neighbor algorithm. Then, a multi-step stitching heuristic is applied to recombine these segments in a manner which can handle not only missing but also false detections. The voxel-wise labelling is then retroactively corrected to include the missing segments, and to successfully label the fiber boundaries which are a source of frequent error for ML tools. The method is shown to be effective across many material compositions (filling ratios), with close to no human input, except at the ML model training stage.

The material specimen under consideration here are produced by free-space extrusion (3D printing nozzle not pressed against the build plate, but extruding in air). This way, phenomena present at the meso scale (inter-bead and inter-layer voids, over- or under-extrusion) and macro scale (infill fraction, infill pattern, stacking of layers of different relative orientation, etc) [17, 18, 21, 63] are removed from consideration, allowing an analysis of the morphology at the microscale in a more pristine state.

3.1. Specimen preparation

Pellets of PEEK 90G (Victrex™, UK) were first desiccated in a Cole-Parmer 282A Vacuum Oven (Antylia Scientific, USA) at 150°C for 5 hours. For each specimen, pellets were first introduced in a DSM Xplore Micro 5 cc twin-screw microextruder (Xplore Instruments BV, Netherlands), before introduction of Panex™ 35 Type 83 chopped CFs (Zoltek, USA), with weight fractions from 5 to 40%, by 5% increments (pure polymer was removed from consideration as it shows no porosity and doesn't require tracking). Mixing (while extrusion is shut off) was carried out at a constant speed of 3 mm/s at 360°C. Extrusion was made at a constant speed of 3 mm/s at 390°C. Only sections of the filament with a variation of 100 microns or less as measured with a caliper were kept for extrusion in a 3D printer extruder. Printing of specimen was performed on a AON3D™ industrial 3D printer, extruding through a 0.6 mm diameter nozzle in free space (not pressing on the build plate) with a nozzle temperature of 390°C. The resulting average specimen diameter is 500 μm.

3.2. Tomographic data acquisition

Individual filaments specimens were then mounted on a pin vise and placed in a ZEISS Xradia™ 520 micro-computed tomography system. Each specimen was exposed to a source power of 80 KV, with the source at a distance of 10 mm, and the detector at 15 mm, with no filter in the beam line. 1600 projections were acquired for each specimen, for a total acquisition time of ~1.75 hour per specimen. Volumetric reconstruction was performed with the parameters obtained automatically by the Zeiss Reconstructor™ software. The resulting voxel dimension is 0.7 μm, and the filaments were entirely inside the scanned field of view. Figure 1a shows a sample 2D slice of the resulting tomograph, for a PEEK filament (diameter 0.6 mm) with 40 wt.% CF. In Figure 1b we can see that the pores (large dark structures) have a light region at their boundary which has the same grey intensity as the fibers (smaller white round shapes), complicating the segmentation task. These artifacts are attributed to sharp changes in refractive index in the specimen, and could be attenuated by imaging in phase-contrast mode, in which source and detector are much farther apart [64]. However, this incurs much longer and therefore more expensive scans.

While OpenFiberSeg can work on larger specimen sizes (up to 1.4 mm in diameter, using 4500 projections and a total exposure time ~4 hours), with the contrasts encountered with CF PEEK, pixel sizes >1 μm lead to unsatisfactory performance of InSegt, for which the stitching procedure cannot compensate. This means highly resolved scans are required for this class of materials. Although not presently tested, glass fibers (GF) reinforcements would have a stronger imaging contrast, as they are mainly made of silicon rather than carbon atoms like polymers, have a density of 2.61 $\mathrm{g/cm^3}$ compared to CF at 1.72 $\mathrm{g/cm^3}$ and average diameter of 12 μm against 7 μm for CF [12]. In which case, larger pixel sizes (up to 2 μm) will probably be acceptable.

3.3. Global processing flowchart

The data processing is structured in the manner illustrated in Figure 2. Starting form the tomographic data, the phases are separated on a voxel-by-voxel basis. Then, for all three reference directions x, y and z, individual fiber regions are separated, and centroids extracted. Tracking of fibers is performed, including stitching of partial detections. From fiber tracks, 3D representations of each fiber are constructed, with gaps identified by the stitching procedures

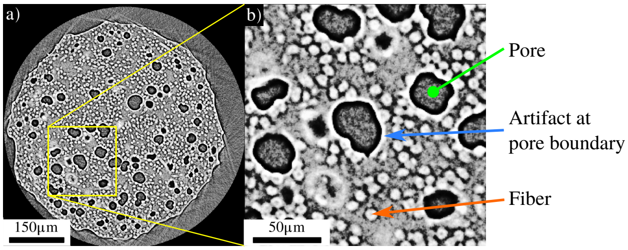

Figure 1: Sample 2D slice of tomographic scan of a PEEK 40 wt.% CF filament (after histogram equalization). a) Entire filament cross-section b) Pores and fibers are indicated by arrows, along with the artifacts in the region surrounding pores.

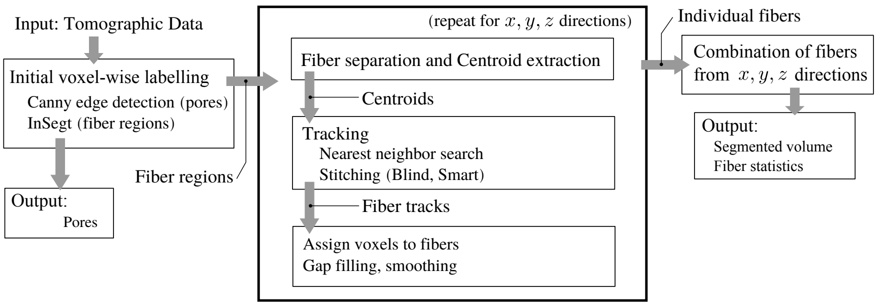

Figure 2: Schematic flowchart of the segmentation and tracking procedure. From the tomographic data, voxels containing pores and fibers are first isolated, then fibers are tracked and reconstructed from all 3 reference directions, to be combined in a single segmented microstructure.

filled. Fibers detected from all 3 directions are then recombined to form the final segmented output. The entire procedure requires minimal input from the user, and accomodates a variety of material types (continuous fiber composites, and FFF SFRP of very different filling ratios, etc). The relevant parameters are scaled with respect to the voxel physical dimension, which depend on scanning parameters.

3.4. Initial voxel-wise labelling

3.4.1. Porosity detection

The first labelling steps consists in identifying which voxels contain either polymer matrix, fiber reinforcement, porosity, or are outside the filament (the perimeter). First, the contrasts in the raw data are enhanced using histogram equalization from the OpenCV library (cv.equalizeHist). Then, with the help of the Canny edge detection algorithm (implemented in the Scikit-image library [65]), both the perimeter and the porosity can be identified on each 2D slicing of the volume. This algorithm uses the gradient in the image and two thresholds to identify continuous contours. To identify the perimeter, a binary mapping is first created by thresholding the image with Otsu's method. This mapping makes the specimen stand out from the perimeter, and the boundary is easily identified. The Canny algorithm is used twice: on the binary mapping (to find the specimen boundary), and on the original histogram-equalized image (to identify pore boundaries). The required parameters for the Canny algorithm depend on image characteristics. For the datasets used in this study, the following parameters were used: low_threshold ranging from 60-100, high_threshold

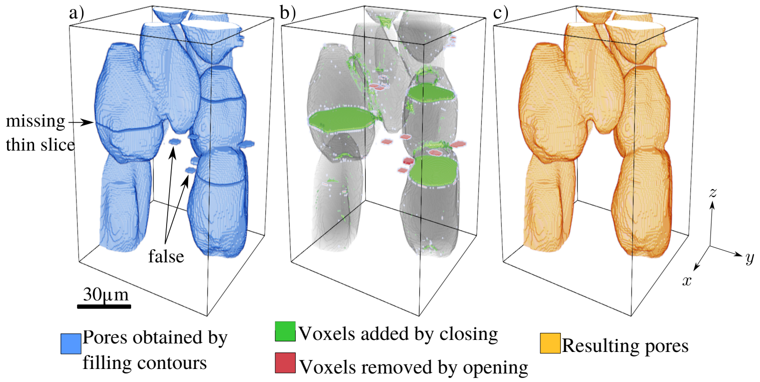

Figure 3: Porosity labelling, typical region of data (2D slicing in $x-y$ planes): a) as obtained by filling the closed contours of the Canny algorithm. b) Morphological closing fills in missing thin slices inside well-defined pores, opening removes false detections. c) Resulting pores.

of 180-200, and sigma=3.0 for the porosity detection, and low_threshold=30, high_threshold=50 and sigma=1.0 for perimeter detection. See attached source code for further details. In order to fill in the closed contours in each case, the floodfill algorithm (cv.floodfill) is used, which labels all the voxels reachable (not bound by a closed contour) from a given seed point. The Canny method was favored over simpler gradient-based methods like Sobel, Roberts or Prewitt edge detection as it more robust against noisy data [66] and it produced closed contours consistently amidst the variety of edge characteristics encountered in the original data. As can be seen in figure 1b, pore edge sharpness can vary significantly, making simpler methods unsuitable.

Figure 3a shows the result of the porosity extraction by contour filling in a typical region of data. Because the contours are at times too attenuated in a few (typically 1-2) image slices, the volume of pores are interrupted by a few thin missing sections. Small regions are also present, which visual inspection reveals to be false positives (the smallest real pores are much larger than these structures which are <2 μm thick.)

As shown in Figure 3b, both types of artifacts are eliminated by performing the 3D morphological operations of **closing** (filling in missing thin slices) and **opening** (removing structures smaller than the structuring element) as implemented in the N-dimensional image processing library SciPy.ndimage [67]. For both operations, spherical structuring elements of radius 3 and 1 voxels are selected, respectively. These are large enough to handle the encountered artifacts, and small enough to leave the general topology of pores unaffected. The resulting pores after corrections are shown in Figure 3c. Relying on classical image processing such as this has the advantage of handling a variety of scanning conditions and morphologies without any intervention, or occasionally requiring the adjustment of a handful of parameters (the two Canny thresholds), rather than the re-training of neural networks encountered in ML. We therefore elected to not investigate ML methods for this particular task.

3.4.2. Fiber detection and separation into convex blobs

The InSegt tool is used to find probable fiber-containing regions. In InSegt, a manual labelling of a small region of the data is used to create an image dictionary based segmentation tool using the machine-learning method called K-means clustering. A specimen image slice is then processed, yielding a probability field giving the likeliness that each voxels belongs to a fiber or not. By inspecting this probability field, the user selects a threshold above which to label pixels as fibers, and checking against the input to ensure the majority of fibers are found, with as little false positives as possible. The full volume is then processed to obtain an initial mapping of all voxels containing fibers. For specimen with low filling fraction (<15 wt.%), the fiber regions were often underestimated in size, because setting the threshold lower to capture the whole perimeter for each fiber also introduced many false detections. This minor effect was corrected with a method presented in Supplementary Materials, involving the Laplacian of the probability field.

As shown in Figure 4a, each voxel is now considered either matrix, pore, or fiber. However, the InSegt tool often labels fibers in close proximity as a single connex region, or *blob*. To identify individual fibers across the volume, it is necessary to detect the regions containing more than one fiber, and split them accordingly. First, the watershed algorithm is used to find all the connex regions (using the cv.watershed function, implemented in the manner detailed in [68], with distance parameter of 0.8 pixel). Then, OpenCV functions cv.findContour and cv.convexityDefects are then utilized to flag the blobs that are not convex (defined as a convexity defect size >1.2 pixels). The blobs passing or failing this convexity test are represented in Figure 4b as "single fiber" blobs and "rejected" blobs, respectively. To reprocess the "rejected" blobs, the watershed transform is used again, in a recursive manner: the distance parameter of the watershed is increased by 0.1 pixels increments for each individual blob. When the new watershed transform outputs more than one blob, the convexity test is performed on those new blobs. New blobs that are flagged as non-convex are then processed by themselves in the same manner. The resulting subdivision of each blob into the largest number of convex blobs is illustrated in Figure 4c. For these individual fiber blobs, a centroid (analogous to center of mass) is computed with the OpenCV function cv.moments, as shown in red in Figure 4d. Note that not all identified centroids belong to real fibers, as some will be false detections, particularly due to light-colored artifacts around pores. The shape of these artifacts is such that those centroids will most likely not form neatly defined chains of sufficient length, and they will be discarded during the tracking procedure.

The fact that detection of pores and perimeter, the splitting of blobs, the convexity tests and the extraction of centroids can be done on a slice-by-slice basis allows these step to be done in parallel, yielding a speedup factor equivalent to the number of cores available.

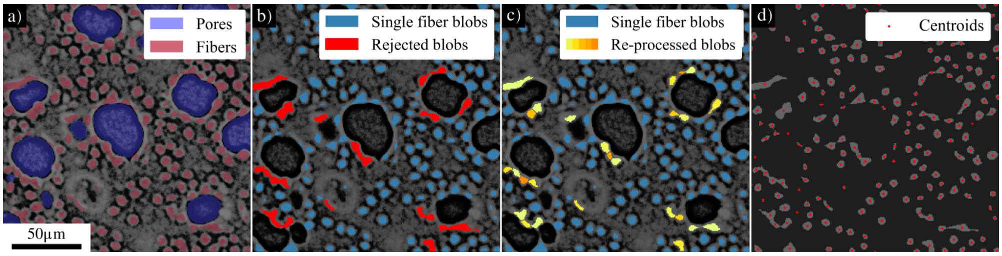

Figure 4: Initial labelling and centroid extraction in data from a PEEK 40 wt.% CF specimen. a) Labelling of pores by Canny edge detection and fiber blobs with InSegt. b) Fiber-containing blobs failing convexity test flagged for reprocessing. c) Output of recursive watershed transform on non-convex blobs. d) Extraction of centroids for each fiber blob.

3.5. Tracking

Figure 5 shows a schematic of the entire tracking procedure: image slices are imagined as 1 dimensional (1D) projections, shown as dotted lines. Fiber regions were identified (with some missing and false detections, as shown in Figure 5b, and centroids were extracted, from which complete fiber objects are sought. When tracking in the vertical direction, the fibers roughly aligned with this direction will have centroids on adjacent slices at a small distance in the transverse plane, when compared to the radius of the fibers. For each pair of adjacent slices, we want to find the pairs of centroids that are mutually closest. The K-nearest neighbor (KNN) algorithm is very efficient and highly scalable in this setting, as it can find the closest neighbor with an $\mathcal{O}(n \log n)$ complexity. For each slice, a K-dimensional tree (KD-tree) is built (in 2D, for x and y coordinates), as implemented in SciPy. The KD-trees are then queried at the coordinates of the centroids for the following slice. We then initialize fiber objects from the continuous chains of closest centroids: centroids on the first slice which are successfully paired to those on the second form initial fiber segments (if they are within a maximum distance). From then, centroids on the following slices are either matched to an existing fiber, to which they are added, or become new fibers themselves, as depicted in Figure 5c.

3.5.1. Blind stitching

Due to missing and false centroid detections, the centroid chains are often interrupted segments from a single true fiber. Using only the start- and end-points for each chain, a similar procedure is done: a 3-dimensional KDTree is constructed for the start- and end-points. Both trees are queried with the other set of points, and matching nearest neighbors are found. Three checks are made before selecting fibers for combination: these matches need be below a prescribed distance, set empirically to 2.5 fiber diameters for CF (or 20 μm) in the stitching direction, and 1 diameter (7.5 μm) in the transverse direction, as well as to not allow backtracking: the end-point of the lowest fiber must be lower in the z direction than the start-point of the higher one. The distance criteria are taken relative to the fiber diameter, which can be measured visually if not known for a particular material. These values allows for some imprecision in the centroid position relative to the true fiber center, without allowing a match to a different fiber that is neighboring the main one. The matching pairs that meet these criteria are combined, linking the corresponding centroid chains. As

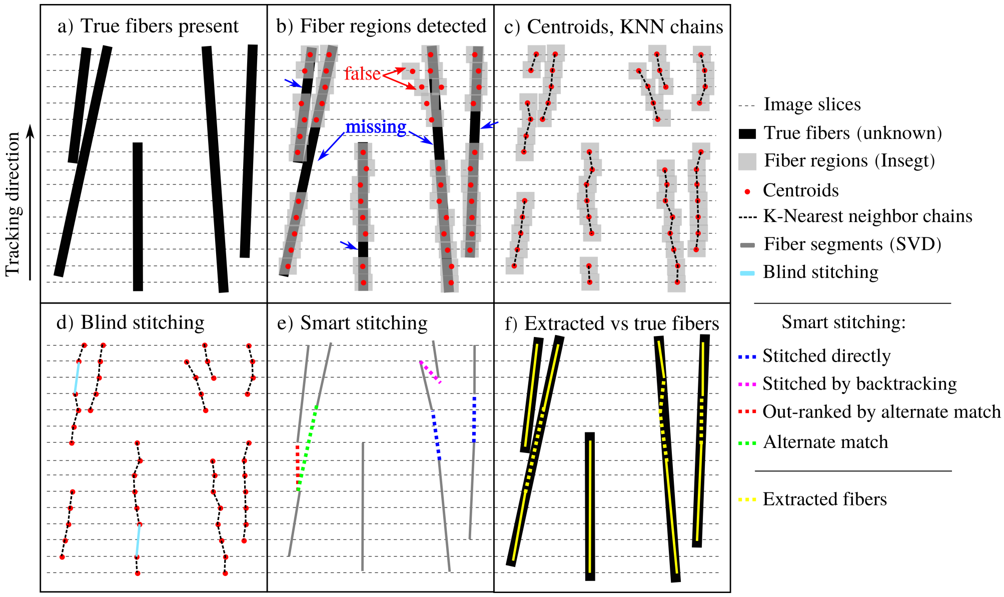

Figure 5: Schematic representation of fiber tracking: a) true fibers in the data (unknown). b) Detections by InSegt, with missing and false regions. c) Extracted centroids, linked in chains of nearest neighbors. d) Blind stitching: bridging small gaps of few missing centroids (light blue). e) Fiber segments that are sufficiently aligned in space are combined (blue). Segments that overlap can also be stitched, if backtracking length is below a maximum distance (shown in pink). When more than one stitching candidate is found, better alignment between longer fibers is favored (in green) over first match (in red). f) Extracted fibers overlaid on true (unknown) fibers in data.

we can see in Figure (5)d-e, for each centroid chain a line segment is obtained that represents its main orientation and length, by the singular value decomposition (SVD) method (numpy.linalg.svd function).

The limitations of the "blind" stitching method are that if a long gap is present in the data for a particular fiber, there isn't enough information to ascertain that the detected segments are really part of the same fiber, or if there are two distinct fibers that are somewhat aligned. Large gaps attributable to many missing centroids are likely to occur in two contexts: in the vicinity of pores, and when fibers that have strong inclination (>45°) relative to the main direction, with an elongated cross-section. Both of these effects lead to interruptions in fiber tracking. With blind stitching alone, an underestimation of long fibers would occur, and since longer fibers contribute the majority of the mechanical load transfer, they are quite significant, especially for those at a strong inclination. To circumvent this limitation, the following method is employed.

3.5.2. Smart stitching

For each fiber segment (shown in grey in Figure 5e, two six-dimensional vectors are constructed (one for each end-point): the 3 coordinates of the point, and the 3 components of its normalized orientation vector. Then, a 6-D KDTree is constructed for the end (topmost) points vectors, and the start (lowest) point vectors are the query points. This way, as shown in blue in Figure 5e, we simultaneously find the pairs of objects that are closest both in terminal point distance and in terms of relative angle. Here it is possible and desirable to allow the stitching of segments that exhibit backtracking: segments belonging to the same fiber overlap each other quite often, due to the presence of erroneous centroids along the path of the fiber. As shown in purple in Figure 5e, allowing the stitching of fiber segments that overlap up to a maximum prescribed distance can be done reliably by assuring that both the relative angle and the start-to-end transverse distance (in the plane normal to the main direction) are sufficiently small.

As shown in red in Figure 5e, sometimes a match is made first which satisfies requirements in distance and relative angle, but an alternate match (in green) is also possible, perhaps further away, but with a more perfect alignment. When instances of this scenario were encountered in the real data, predominantly the offending candidate was a short segment, in the vicinity of the endpoint of the main fiber. To avoid these false matches, a ranking function was devised that favors stitches between longer segments (the orientation vector has more statistically significance for a higher centroids count) without deteriorating the relative angle by more than a prescribed value. This way, from all possible candidate matches for a particular segment, the ones between longer segments at acceptable relative inclination were prioritized.

By checking not only the endpoint distance but also relative angle, the distance criteria can be set larger than for the "blind" stitching step, without risking the stitching of non-related fiber segments. Once all segments to be stitched have been identified, two additional checks are made: in the gap between the endpoints that would be connected by the stitching, new centroids are interpolated at each of the z coordinates corresponding to an image slice. Above a certain distance, to avoid connecting fibers which truly aren't related, a majority of those new centroids must be in a region which was labelled as "fiber" by the InSegt tool (rather than "pore"). Secondly, none of the new centroids can be at a distance of less than one fiber diameter from an existing fiber, as they would otherwise physically overlap with the existing fiber. If both tests are passed, stitching is allowed and the interpolated centroids are inserted in the gap between segments. Once all the stitching steps are complete, we update the fiber line segments to account for the presence of partial segments and interpolated centroids.

The fiber objects that have a length below a prescribed minimum are marked as "rejected". Many false positives occur at very short fiber lengths, when a few non-related centroids are connected, but do not represent a real fiber in the data. A length of 1 fiber diameter is chosen as the minimum permissible length, and fibers shorter that that are marked as "rejected". Since the mechanical behavior will be determined mainly by longer fibers, missing a few real fibers at such short length is considered acceptable, so long as the fiber filling fraction remains close to the known value for the material in question. Fibers with strong inclination ($> 55°$ from tracking direction) are also rejected, as they will be more accurately tracked along the direction with which they are most aligned with. (A vector $[1, 1, 1]^T$ forms an angle of 54.7° with any of the reference axes, so a larger angle indicates better alignment with another axis). By performing the entire centroid detection and tracking procedure from the 3 reference directions (x, y, z), all possible inclinations are thus captured.

3.6. Assigning voxels to fibers

To reconstruct the fiber bodies from the identified centroid chains, we link voxels in the initial labelling to each of them. For the majority of voxels in the watershed output, assigning a fiber ID number is immediate, as the tracked centroid was obtained from these voxels. However, in the gaps between stitched fiber segments, the centroids created by interpolation are not related to any existing voxels. For those cases, the first step is to check whether the interpolated centroids are squarely inside a closed contour that is not already matched to another fiber, in which case all those voxels are assigned to its fiber. If more than one centroid (either interpolated or present in the initial extraction) are present in the same closed contour, the watershed transform is used to assign the voxels to the closest centroid, assuring the subdivided voxel groups all lie in a single connex region. Remains the case where interpolated centroids lie in regions where no voxels are labelled as fiber. To create this labelling, the following method is used.

3.7. Volumetric post-processing: gap filling and artifact removal

As shown in Figure 6a, for each fiber identified in tracking, a sub-volume is created which is only large enough to contain the voxels belonging to that fiber. A tube-like structuring element is created by stacking 2D circles (of the same diameter as a fiber) at the same angle and direction as this fiber's orientation vector, for a total height of a few voxels longer than the largest gap created by stitching (or a default value for unstitched fibers). The morphological operation of closing (scipy.ndimage.binary_closing function) is applied using this structuring element. As shown in Figure 6b, this has two effects: it smooths the surface of the fiber, and it fills gaps in a manner that is inferred from existing geometry, rather than prescribed. This is preferable because some fibers have an oblong rather than a circular shape, which this method preserves. Also, strongly inclined fibers will have elongated cross-sections. The morphological operation of opening (scipy.ndimage.binary_opening) is used afterwards with a ball structuring element, with a diameter slighly under a fiber diameter. The effect of this is to remove the regions that are erroneously labelled as belonging to this fiber: just for like pores, these false detections will be thin, and are readily removed by opening. In Figure 6c, we see the topmost regions of the fiber after removal of such an erroneous shape (i.e., an artifact).

Making this operation on a subset of the entire volume is memory-efficient, and can be done in parallel. A last check is made when projecting it back into the large volume: newly identified voxels should not spill into regions already identified as another fiber, or a pore.

In Figure 7, we can see the effect of the morphological operations on several fibers at once, in a small region of interest. In Figure 7a) are presented the fibers as obtained by tracking and assignment of voxels. We can see interruptions of different sizes, as well as the same erroneous structures previously seen. In Figure 7b the effect of closing and

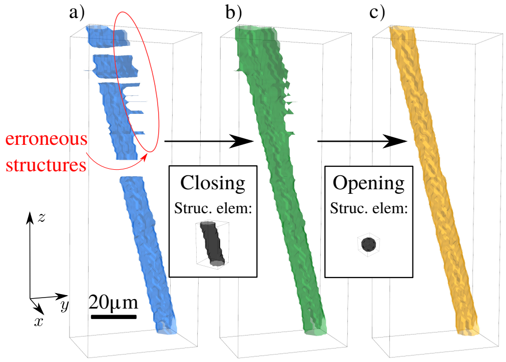

Figure 6: Example of post-processing on a single fiber object made up of 4 stitched segments, leaving three gaps (tracking performed along z). a) Fiber from previously labelled voxels, including erroneous structures. b) Output of morphological closing with inclined rod structuring element: gaps are filled, but erroneous regions are expanded. c) Output of morphological opening with ball structuring element: smoothing, removal of erroneous regions.

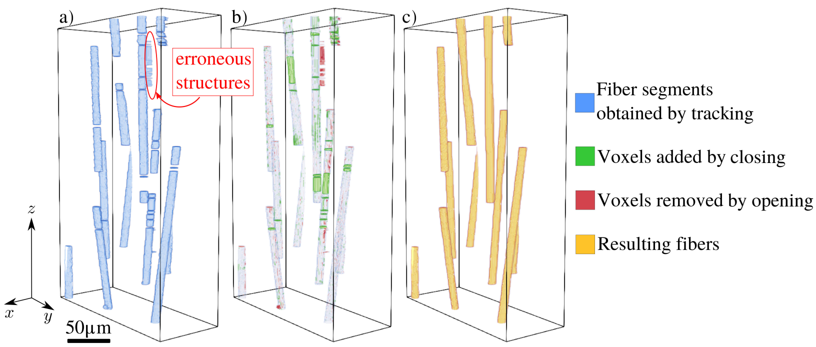

Figure 7: Post-processing applied to a larger region showing several distinct fiber objects. a) Fiber segments as obtained by assigning voxels to the tracking output, with several gaps. b) Morphological closing adds missing segments where interpolation has occurred, and opening removes a few erroneous structures. c) Resulting volume of fibers.

opening are highlighted: closing fills in the gaps between interpolated segments, opening removes erroneous regions. The resulting fibers in Figure 7c are a much more reliable representation of those present in the data.

3.8. Combining fibers from all reference directions (x, y, z)

As strongly inclined fibers are more easily detected by slicing in the transverse plane (x and y directions), the entire segmentation procedure explained above is repeated twice more. Using the labelling obtained in the direction of main alignment (z), all voxels where fibers were successfully identified (and not rejected for being too short or too steep) are first removed from the pre-segmentation volume (substracted from the InSegt output). This way, only new fibers can be found.

After the entire procedure is performed for both x and y directions, the fibers found need to be projected onto the original frame orientation. The most problematic cases are long fibers which are inclined by close to 45° to more than one of the reference directions. This results in partial capture of segments from potentially all three reference frames, which for the x and y directions can potentially interfere with each other. Two more steps are taken to correct

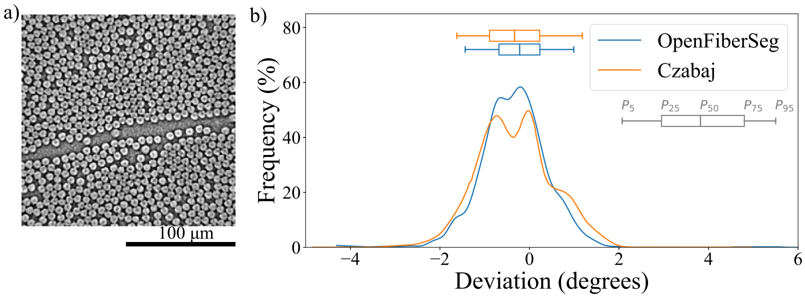

Figure 8: Extraction performed on original micro-CT scan of unidirectional graphite/epoxy composite. a) Sample data slice, reproduced with authorization [51]. b) Probability density function of fiber deviation from main direction, as reported by original authors, and as measured with OpenFiberSeg. The box and whisker plots for each peak represent the 5th, 25th, 50th, 75th and 95th percentiles for both segmentation methods, which are all within 0.5°, indicating good agreement between the methods.

these problems. First, colliding voxels are identified and if their corresponding fiber objects are sufficiently aligned, the objects are combined into a single fiber. Then the smart stitching method is called on all the fibers from all the permutations, with the provision that only fibers from two different permutations are eligible to be stitched together. This allows the reconstruction of fiber whose segments were obtained from more than one reference direction. Finally, the volumetric post-processing method is applied again on the fibers that have been combined or stitched in this last step, yielding the final segmentation of fibers present in the data.

4. Validation

The segmentation procedure was performed on 2 distinct datasets, whose analysis were previously published by Czabaj [51, 58] and Creveling [52], and kindly made available to us. By performing the segmentation on the same input data, we can compare our tracking results to theirs, and verify the degree of accuracy of OpenFiberSeg for the type of materials on which these scans were performed. The code from these two projects not being public, only the results in the original publications can be discussed.

4.1. Data from Czabaj et al, 2014

This dataset is obtained from a specimen of AS4/35016 graphite/epoxy unidirectional composite, formed into a thin "matchstick" specimen. The resulting tomograph is presented in Figure 8a. The authors of this work used template matching and a sophisticated method involving the Kalman filter and track stitching to track fibers across the volume, and preventing fiber inter-penetration [51, 58].

As can be seen in Figure 8b, the shape of the histograms of angles measured with our tool vs that in [51] are quite close, especially when considering the position of the 5th, 25th, 50th, 75th and 95th percentiles, which are all within less than 0.5° between our results and theirs. While the height of the central peak is 9% higher for our method when compared to theirs, several reasons can account for this. When obtaining fiber centroids at each slice, we compute

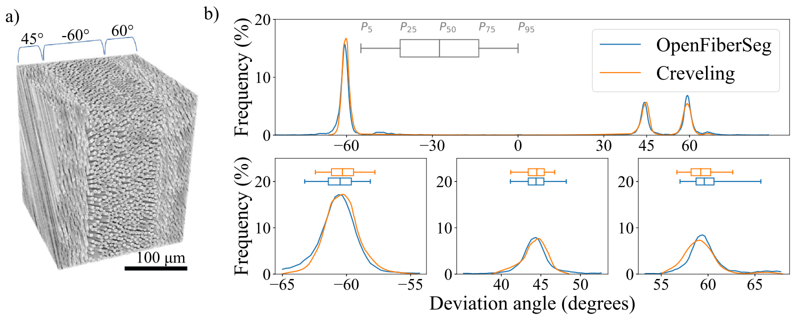

Figure 9: Extraction performed on micro-CT scan of carbon/epoxy laminate. a) rendering of original data, showing the main angles of the three layers, relative to the vertical direction [52]. Reproduced with authorization. b) Probability density function of fiber deviation from main direction, as reported in [52], and as measured with OpenFiberSeg. The bottom portion shows zoom around the three main peaks, with generally good agreement between the output of the two methods. The box and whisker plots for each peak represent the 5th, 25th, 50th, 75th and 95th percentiles for both segmentation methods, when grouping the data around the three main peaks.

the moments of the fiber blobs, whereas their methods finds the best match for a pre-defined circular template: some variability in centroid positions is likely to occur between the two methods. Secondly, when attempting to reproduce their results, we needed to truncate the dataset as they did, leaving 508 out of 629 fibers, without knowing the exact coordinates. Also, while all fibers presented are found automatically in OpenFiberSeg, in the original paper manual segmentation of 4 missed fibers, and removal of 3 false one was done. They report a processing time of 2 hours on a CPU capable of 4 simultaneous threads. Our method also executes in 2 hours when using 4 threads.

4.2. Data from Creveling et al. 2019

This data was obtained on a IM7/8552 carbon/epoxy laminate, from which a 1 mm^3 specimen was extracted. A high-resolution micro-CT scan was performed, yielding a voxels size of 0.41 μm. As shown in Figure 9a, this specimen has 3 plies, with fibers oriented at +45°, -60°, and +60°, as measured from the vertical direction. In the original paper, the fibers were extracted using template matching and a more elaborate method of stitching. As can be seen in Figure 9b, there is only small deviation between the outputs of our method and theirs, especially when considering the position of the percentiles for each peak. The remaining difference in peak heights can probably be explained by the different method of obtaining centroids, i.e. template matching vs the direct calculation of center of mass of irregularly shaped blobs, used in out method.

From these two analyses, we can assert that OpenFiberSeg of segmentation yields very similar results to state-of-the art tools, at least when it comes to the tracking of fibers in bi-phasic, continuous fiber reinforced polymers. As we will now show, OpenFiberSeg can handle a much larger number of fibers, with more randomness in orientation (hence more contact between fibers) and to produce accurate results from partial detections, amidst porosity.

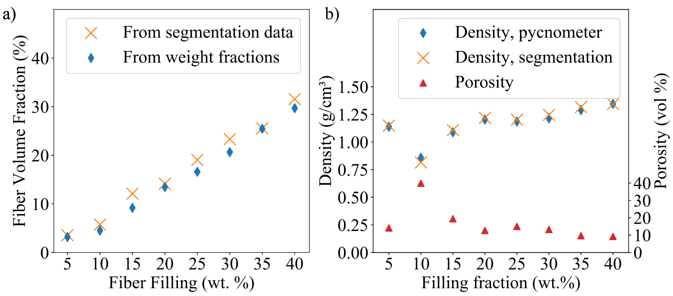

Figure 10: Experimental validation: a) Comparison of fiber volume fraction obtained directly from the segmentation output, vs. calculated from the known densities of matrix and reinforcement materials, as a function of fiber filling fraction. The difference between the two is at most 4% (meaning if one method gives 10%, the other can give at most 14%). b) Comparison of specimen density, as calculated from the segmentation output and the density measured directly with the help of a gas pycnometer. Very high agreement (mean error <2%) between the two indicates the proportions of matrix, fiber and porosity as predicted by the segmentation are a reliable indicator of the proportions in the real material.

5. Results

5.1. Predicting fiber volume fraction and material density

For SFRP with several tens of thousands of individual fibers, getting a clear appreciation of the quality of the segmentation is not straightforward. One way is using the segmentation data to predict properties such as the specimen density or the fiber volume fraction c_f^v and compare them to values measured experimentally. The c_f^v is obtained directly from segmentation data, and can be calculated experimentally from the knowledge of the mass fractions used at the specimen preparation step, fiber and matrix density (from supplier data), and the pore volume fraction c_p^v measured by OpenFiberSeg. To independently validate that the segmentation tool produces the correct assessment of porosity, the total density of each SFRP specimen is calculated, and compared to the measured experimental value of density. Detailed calculations are presented in Supplementary Materials.

As shown in Figure 10a, there is generally good agreements between fiber volume fractions as predicted from the segmentation output and those obtained by the mass fractions. The results from the segmentation output are overestimated by at most 4% for some filling fractions. This variation can be explained considering how different are the morphologies from low to high filling fractions (with porosity ranging from 10% to 40%), and the fact that no tweaking of parameters is done to process them.

As shown in Figure 10b, the two methods of determining density are in high agreement (mean error of <2%), which would only happen if all the volume fractions were correctly estimated, particularly c_p^v, which has a larger effect on density, as pores occupy space but contribute no mass. Any remaining deviation between the two density measurements can be explained by sampling error: the tomographs encompass a volume of 1 mm^3, while the specimen used for the pycnometer measurement is ~200× larger. The scanned region might possibly have a local phase distributions slightly different from the average. The much higher porosity (39%) of the 10 wt.% CF specimen explains the large departure

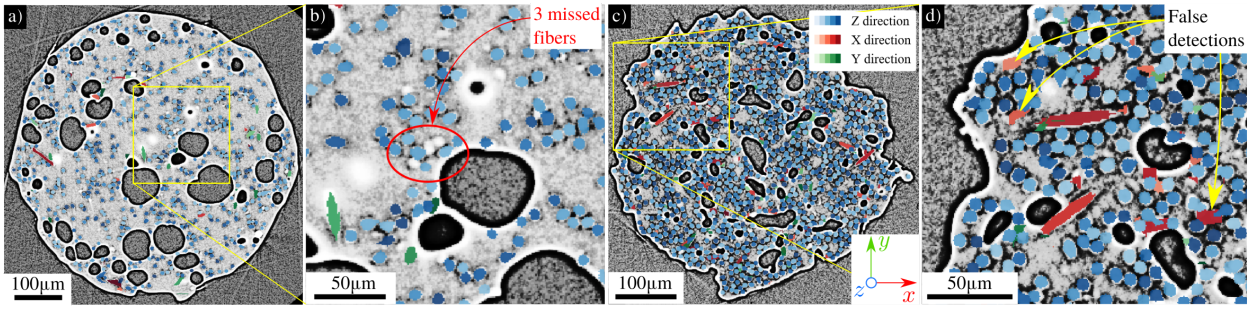

Figure 11: Output of segmentation for 2 material compositions: a) PEEK with 15 wt.% CF and c) with 40 wt.% CF. Different color maps are used to represent in which reference direction the fiber was detected. The majority of fibers are detected in the out-of-place (z direction), and some in the in-plane directions x and y. In b), a closer look shows examples of missed detections, and in d), we can observe that more false detections are present in the x direction, but the strongly inclined fibers are also successfully captured.

of it's density from the general trend. It can also explain the largest discrepancy between both methods, at 4.9% error: possibly some helium leaks into the unusually large pores, leading to an overestimation of density from the instrument. Ning *et al.* also reported an uncommonly high value of porosity for 10 wt.% CF filled acrylonitrile butadiene styrene (ABS) (9.04% whereas specimen with 0-15% filling averaged at 2%) [31].

It remains possible however that the volume fractions are accurate on average, but only due to the number of missed fiber detections being cancelled by false detections. To ascertain how reliable the output at the pixel level, the following method is used. On a slice-by-slice basis, we can superimpose the segmentation output onto the raw data. This visualization is presented in Figure 11 for two different material composition: in a) PEEK with 15 wt.% CF and in b) PEEK with 40 wt.% CF. A different colormap was used to show which reference direction each fiber was detected from. For both these materials, it is clearly visible that the vast majority of fibers present are identified, with only a few missed fibers or false detections. Also, nearly full cross-section of each fiber is captured rather than a portion of it. And while there are more false detections in the in-plane directions (as shown in Figure 11d), the fibers with strong inclination (near-tangent to the $x - y$ plane) are also successfully captured. To assess the segmentation precision, a slice-by-slice analysis is presented in Video 1 for the specimen with 25 wt.% CF. For each studied slice, we compared the fibers detected by OpenFiberSeg against the original data, and labelled false fibers or single true fibers fragmented into segments as false positives (FP) and missed fibers or separate true fibers combined into one as false negative (FN). This annotation is performed at 7 separate locations (2D slices) in the data, encompassing 3945 individual fiber detections. Precision for this specimen (defined as the voxel ratio of TP/(TP+FP)) is computed to 95.6%, with rates of FP of 4.4% and FN of 1.6% (average across all filling ratios: precision: 93.1%, FP: 6.9%, FN: 1.5%). The majority of FP are in the vicinity of pores, and are for short fibers (<20 μm). Overall, there is <1% occurence of fiber fragmentation or false combination.

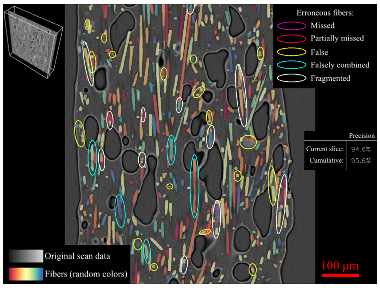

Video 1: Slice-by-slice analysis of segmentation accuracy: PEEK 25 wt.% CF. The porosity and perimeter detection are shown to be nearly perfect. The fiber extraction precision is measured at 95.6% for this specimen. Animated sweep of fibers colorized first by length and then deviation highlight the trend by which longer fibers are better aligned and vice-versa.

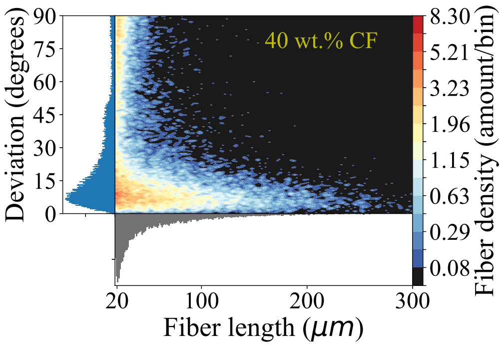

Figure 12: 2D histogram representation of the correlated lengths and angle of deviation from tracking direction (z) for fibers present in a PEEK specimen with 40 wt.% CF filling ratio. Single-variable histograms are juxtaposed on the left-hand and lower side, to highlight the relationship between the counts for each variable and the correlated density values.

5.2. Discussion

For each material specimen, we obtain a set of individual fibers, complete with their position in space, orientation vector and length. In order to study the correlated distribution of lengths and orientations, and to compare them across material composition, we produce the following visualization. In Figure 12, a 2D-histogram is presented for the fibers present in a PEEK specimen with 40 wt.% CF. The lengths and deviation angle are both discretized into 256 bins, and the color of each pixel represents the density (amount/bin) for that combination of length and deviation angle. A logarithmic scale is used for the colormap, so that both high and low density regions are appreciable. Single-variable histograms for lengths and deviation angle are also shown, making explicit the relation between bin count and the pixel color mapping. The correlated histogram allows us to assert the inverse relation between fiber length and deviation: longer fibers tend to be better aligned, and shorter fibers can deviate more (although the bulk of the distribution is always at <30°). The extent of shear-induced alignment during the extrusion process is thus revealed, which could not have been inferred from the single-variable histograms alone.

The same visualization allows us to compare the specimen between them: in Figure 13, all 8 specimen types are juxtaposed, in order of increasing filling ratio. Fiber counts and processing times on a workstation with an Intel™

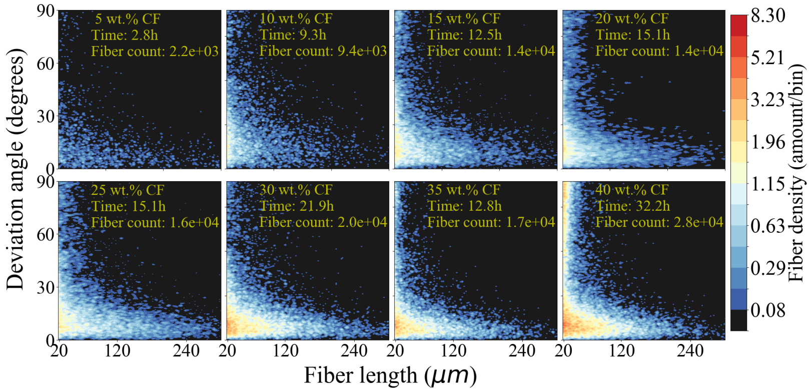

Figure 13: Correlated lengths and deviation histograms for PEEK SFRP with filling ratios of 5-40 wt.% CF. For all levels of filling, there exists an inverse correlation between fiber length and deviation: longer fibers will be more aligned with the extrusion direction. Processing time is given, along with fiber count for each scan.

i9-10940X CPU, and 64GB of RAM are presented for each dataset. Here we can see that the shear-induced alignment is present even at low fiber concentrations. This indicates it is attributable to fibers aligning with the flow direction, more than interactions between fibers which are less frequent at low filling fraction. Also, for higher ratios, the most noticeable increase (regions in red) is in the <100 μm, <30° range, suggesting more fiber breakage at these ratios, as the proportion of fibers 100 μm and longer are essentially the same for 30 wt.% CF and above. The unusually large proportion of short fibers at large deviations for the 40 wt.% CF also suggest more breakage for higher filling ratios. Additionally, the lower fiber count at 35 wt.% compared to 30 wt.% suggests there is less fiber breakage at this filling ratio.

The degree to which shear-induced alignment is more pronounced for longer fibers is illustrated in Figure 14. Here, for each dataset, only the fibers of a certain length are selected (centered at 20 and 100 μm) and the histograms of the deviation angles are compared. Clearly, the general tendency is that fibers tend to align with the flow direction (the bulk of the distribution is always at >30°) but this phenomenon is markedly more prominent as longer fibers are considered. One dataset (10 wt.% CF) doesn't follow this trend, which can be explained by inordinately large porosity for this specimen, probably changing the flow characteristics. The highest peak for long (100 μm) fibers being for the 35 wt.% also indicates less fiber breakage at this filling ratio.

6. Conclusion

In this work, we presented OpenFiberSeg, a tool for fiber tracking and segmentation of individual fibers in tomographic scans of SFRPs. Combining elements from several techniques, we propose original improvements such as retroactive correction of labelling based on fiber reconstruction, as well as a detailed heuristic for stitching fibers from partially detected segments. The method is shown to be robust and satisfactorily reproduces the results of 2 independent

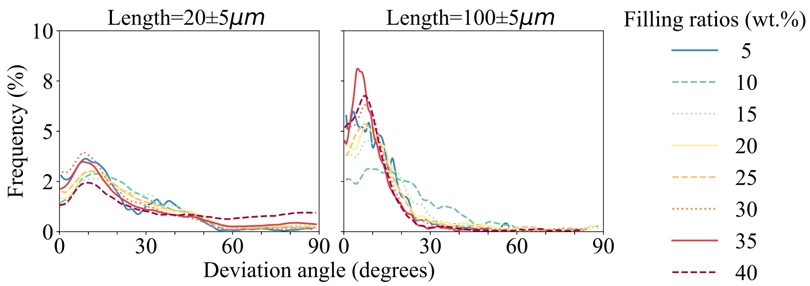

Figure 14: Histograms of deviation angles for 2 different ranges of fiber lengths, centered at 20 and 100 μm, by specimen filling fraction. Shear-induced alignment is present for all specimen, as evidenced by the bulk of the distribution being below 30° for specimen. This effect is more pronounced for longer fibers for all filling ratios, except 10 wt.%, which can be explained by unusually high porosity.

studies on continuous fiber reinforced composites. When applied to FFF SFRP with non-negligible porosity, it can be used to corroborate the experimental measurement of porosity and fiber filling fraction, and produce a detailed portrait of the correlated fiber lengths and orientation distributions for vastly dissimilar specimen composition (5-40 wt.% filling ratio), yielding an average segmentation precision of 93.1% on a per-voxel basis. This tool can serve as a central characterization and diagnostic method for the development of FFF SFRP materials and processes. However, it is not designed for fibers with significant curvature, as fibers are represented by line segments, and up to 1% of fibers can be fragmented or combined with another with which they are well aligned and in close proximity. By divulging the source code, this project can reduce development time for other research groups, and be applied to a variety of use cases, such as other types of SFRP, reinforced ceramics, concrete, etc. The precise knowledge of reinforcement and pore size and position will be invaluable for the development of models involving elasticity, viscoelasticity, fracture dynamics, and transport phenomena.

7. Source code and data repository

The full source code repository along with original tomographic data used in this work are available at `https://github.com/lm2-poly/OpenFiberSeg`.

Acknowledgements

This research project is made possible by financial and technical support from Safran S.A. (FACMO Research Chair), as well as financial support from the Natural Sciences and Engineering Research Council of Canada (Alexander Graham Bell Canada Graduate Scholarship program, and the Collaborative Research and Development program, grant no CRDPJ514761). Computational resources were made available by Calcul Québec (`www.calculquebec.ca`) and Compute Canada (`www.computecanada.ca`). Research data used for validating the accuracy of our method was shared with us by Pr. Czabaj at the University of Utah.

References

[1] R. Dua, Z. Rashad, J. Spears, G. Dunn, M. Maxwell, Applications of 3d-printed peek via fused filament fabrication: A systematic review, Polymers 13 (2021) 4046.

[2] A. Haleem, M. Javaid, Polyether ether ketone (peek) and its manufacturing of customised 3d printed dentistry parts using additive manufacturing, Clinical Epidemiology and Global Health 7 (2019) 654–660.

[3] L. Ding, W. Lu, J. Zhang, C. Yang, G. Wu, Preparation and performance evaluation of duotone 3d-printed polyetheretherketone as oral prosthetic materials: A proof-of-concept study, Polymers 13 (2021) 1949.

[4] W. Wu, P. Geng, J. Zhao, Y. Zhang, D. Rosen, H. Zhang, Manufacture and thermal deformation analysis of semicrystalline polymer polyether ether ketone by 3d printing, Materials Research Innovations 18 (2014) S5–12.

[5] P. Wang, B. Zou, H. Xiao, S. Ding, C. Huang, Effects of printing parameters of fused deposition modeling on mechanical properties, surface quality, and microstructure of peek, Journal of Materials Processing Technology 271 (2019) 62–74.

[6] H. L. Tekinalp, V. Kunc, G. M. Velez-Garcia, C. E. Duty, L. J. Love, A. K. Naskar, C. A. Blue, S. Ozcan, Highly oriented carbon fiber–polymer composites via additive manufacturing, Composites Science and Technology 105 (2014) 144–150.

[7] R. Gao, J. Xie, J. Yang, C. Zhuo, J. Fu, P. Zhao, Research on the fused deposition modeling of polyether ether ketone, Polymers 13 (2021) 2344.

[8] B. Brenken, E. Barocio, A. Favaloro, V. Kunc, R. B. Pipes, Fused filament fabrication of fiber-reinforced polymers: A review, Additive Manufacturing 21 (2018) 1–16.

[9] M. Rinaldi, F. Cecchini, L. Pigliaru, T. Ghidini, F. Lumaca, F. Nanni, Additive manufacturing of polyether ether ketone (peek) for space applications: A nanosat polymeric structure, Polymers 13 (2021) 11.

[10] L. J. Love, V. Kunc, O. Rios, C. E. Duty, A. M. Elliott, B. K. Post, R. J. Smith, C. A. Blue, The importance of carbon fiber to polymer additive manufacturing, Journal of Materials Research 29 (2014) 1893–1898.

[11] M. Luo, X. Tian, J. Shang, W. Zhu, D. Li, Y. Qin, Impregnation and interlayer bonding behaviours of 3d-printed continuous carbon-fiber-reinforced poly-ether-ether-ketone composites, Composites Part A: Applied Science and Manufacturing 121 (2019) 130–138.

[12] P. Wang, B. Zou, S. Ding, C. Huang, Z. Shi, Y. Ma, P. Yao, Preparation of short cf/gf reinforced peek composite filaments and their comprehensive properties evaluation for fdm-3d printing, Composites Part B: Engineering 198 (2020) 108175.

[13] Stepashkin, D. Chukov, F. Senatov, A. Salimon, A. Korsunsky, S. Kaloshkin, 3d-printed peek-carbon fiber (cf) composites: Structure and thermal properties, Composites Science and Technology 164 (2018) 319–326.

[14] Q. Li, W. Zhao, Y. Li, W. Yang, G. Wang, Flexural properties and fracture behavior of cf/peek in orthogonal building orientation by fdm: Microstructure and mechanism, Polymers 11 (2019) 656.

[15] L. Pigliaru, M. Rinaldi, L. Ciccacci, A. Norman, T. Rohr, T. Ghidini, F. Nanni, 3d printing of high performance polymer-bonded peek-ndfeb magnetic composite materials, Functional Composite Materials 1 (2020) 1–17.

[16] S. Sommacal, A. Matschinski, K. Drechsler, P. Compston, Characterisation of void and fiber distribution in 3d printed carbon-fiber/peek using x-ray computed tomography, Composites Part A: Applied Science and Manufacturing (2021) 106487.

[17] S. Garzon-Hernandez, A. Arias, D. Garcia-Gonzalez, A continuum constitutive model for fdm 3d printed thermoplastics, Composites Part B: Engineering 201 (2020) 108373.

[18] A. Nasirov, A. Gupta, S. Hasanov, I. Fidan, Three-scale asymptotic homogenization of short fiber reinforced additively manufactured polymer composites, Composites Part B: Engineering 202 (2020) 108269.

[19] M. Somireddy, A. Czekanski, Computational modeling of constitutive behaviour of 3d printed composite structures, Journal of Materials Research and Technology 11 (2021) 1710–1718.

[20] W. Gao, Y. Zhang, D. Ramanujan, K. Ramani, Y. Chen, C. B. Williams, C. C. Wang, Y. C. Shin, S. Zhang, P. D. Zavattieri, The status, challenges, and future of additive manufacturing in engineering, Computer-Aided Design 69 (2015) 65–89.

[21] M. Domingo-Espin, J. M. Puigoriol-Forcada, A.-A. Garcia-Granada, J. Llumà, S. Borros, G. Reyes, Mechanical property characterization and simulation of fused deposition modeling polycarbonate parts, Materials & Design 83 (2015) 670–677.

[22] M. Talagani, S. DorMohammadi, R. Dutton, C. Godines, H. Baid, F. Abdi, V. Kunc, B. Compton, S. Simunovic, C. Duty, et al., Numerical simulation of big area additive manufacturing (3d printing) of a full size car, Sampe Journal 51 (2015) 27–36.

[23] M. Teßmann, S. Mohr, S. Gayetskyy, U. Haßler, R. Hanke, G. Greiner, Automatic determination of fiber-length distribution in composite material using 3d ct data, EURASIP journal on advances in signal processing 2010 (2010) 1–9.

[24] D. Salaberger, K. A. Kannappan, J. Kastner, J. Reussner, T. Auinger, Evaluation of computed tomography data from fibre reinforced polymers to determine fibre length distribution, International Polymer Processing 26 (2011) 283–291.

[25] H. Shen, S. Nutt, D. Hull, Direct observation and measurement of fiber architecture in short fiber-polymer composite foam through micro-ct imaging, Composites science and technology 64 (2004) 2113–2120.

[26] S.-Y. Fu, B. Lauke, Effects of fiber length and fiber orientation distributions on the tensile strength of short-fiber-reinforced polymers, Composites Science and Technology 56 (1996) 1179–1190.

[27] T. Mishurova, N. Rachmatulin, P. Fontana, T. Oesch, G. Bruno, E. Radi, I. Sevostianov, Evaluation of the probability density of inhomogeneous fiber orientations by computed tomography and its application to the calculation of the effective properties of a fiber-reinforced composite, International Journal of Engineering Science 122 (2018) 14–29.

[28] S. K. Kugler, A. P. Dey, S. Saad, C. Cruz, A. Kech, T. Osswald, A flow-dependent fiber orientation model, Journal of Composites Science 4 (2020) 96.

[29] G. D. Goh, Y. L. Yap, S. Agarwala, W. Y. Yeong, Recent progress in additive manufacturing of fiber reinforced polymer composite, Advanced Materials Technologies 4 (2019) 1800271.

[30] S. Ding, B. Zou, P. Wang, H. Ding, Effects of nozzle temperature and building orientation on mechanical properties and microstructure of peek and pei printed by 3d-fdm, Polymer Testing 78 (2019) 105948.

[31] F. Ning, W. Cong, J. Qiu, J. Wei, S. Wang, Additive manufacturing of carbon fiber reinforced thermoplastic composites using fused deposition modeling, Composites Part B: Engineering 80 (2015) 369–378.

[32] C. Meola, C. Toscano, Flash thermography to evaluate porosity in carbon fiber reinforced polymer (cfrps), Materials 7 (2014) 1483–1501.

[33] T. Mulholland, S. Goris, J. Boxleitner, T. A. Osswald, N. Rudolph, Process-induced fiber orientation in fused filament fabrication, Journal of Composites Science 2 (2018) 45.

[34] S. Yu, Y. H. Hwang, J. Y. Hwang, S. H. Hong, Analytical study on the 3d-printed structure and mechanical properties of basalt fiber-reinforced pla composites using x-ray microscopy, Composites Science and Technology 175 (2019) 18–27.

[35] A. Badran, D. Marshall, Z. Legault, R. Makovetsky, B. Provencher, N. Piché, M. Marsh, Automated segmentation of computed tomography images of fiber-reinforced composites by deep learning, Journal of Materials Science 55 (2020) 16273–16289.

[36] J. M. Sietins, J. C. Sun, D. B. K. Jr, Fiber orientation quantification utilizing x-ray micro-computed tomography, Journal of Composite Materials 55 (2021) 1109–1118.

[37] M. P. Starmans, S. R. van der Voort, J. M. C. Tovar, J. F. Veenland, S. Klein, W. J. Niessen, Radiomics: Data mining using quantitative medical image features, in: Handbook of medical image computing and computer assisted intervention, Elsevier, 2020, pp. 429–456.

[38] R. F. Agyei, M. D. Sangid, A supervised iterative approach to 3d microstructure reconstruction from acquired tomographic data of heterogeneous fibrous systems, Composite Structures 206 (2018) 234–246.

[39] T. Baranowski, D. Dobrovolskij, K. Dremel, A. Hölzing, G. Lohfink, K. Schladitz, S. Zabler, Local fiber orientation from x-ray region-of-interest computed tomography of large fiber reinforced composite components, Composites Science and Technology 183 (2019) 107786.

[40] J. P. Chiverton, A. Kao, M. Roldo, G. Tozzi, Automatic diameter and orientation distribution determination of fibrous materials in micro x-ray ct imaging data, Journal of microscopy 272 (2018) 180–195.

[41] P. A. Hessman, T. Riedel, F. Welschinger, K. Hornberger, T. Böhlke, Microstructural analysis of short glass fiber reinforced thermoplastics based on x-ray micro-computed tomography, Composites Science and Technology 183 (2019) 107752.

[42] F. Chen, Y. Chen, H. D. Tagare, A new framework of multiphase segmentation and its application to partial volume segmentation, Applied Computational Intelligence and Soft Computing 2011 (2011).

[43] S. Evsevleev, S. Paciornik, G. Bruno, Advanced deep learning-based 3d microstructural characterization of multiphase metal matrix composites, Advanced Engineering Materials 22 (2020) 1901197.

[44] R. Lorenzoni, I. Curosu, S. Paciornik, V. Mechtcherine, M. Oppermann, F. Silva, Semantic segmentation of the micro-structure of strain-hardening cement-based composites (shcc) by applying deep learning on micro-computed tomography scans, Cement and Concrete Composites 108 (2020) 103551.

[45] C. Aguilar, I. A. Hanhan, R. F. Agyei, M. D. Sangid, M. Comer, Void detection and fiber extraction for statistical characterization of fiber-reinforced polymers, Electronic Imaging 2020 (2020) 250–1.

[46] T. Li, M. Comer, J. Zerubia, A connected-tube mpp model for object detection with application to materials and remotely-sensed images, in: 2018 25th IEEE International Conference on Image Processing (ICIP), IEEE, 2018, pp. 1323–1327.

[47] C. Aguilar, M. Comer, A marked point process model incorporating active contours boundary energy, Electronic Imaging 2018 (2018) 230–1.

[48] B. Mlekusch, E. Lehner, W. Geymayer, Fibre orientation in short-fibre-reinforced thermoplastics i. contrast enhancement for image analysis, Composites science and technology 59 (1999) 543–545.

[49] S. Goris, T. A. Osswald, Fiber orientation measurements using a novel image processing algorithm for micro-computed tomography scans, in: Proceedings of Society of Plastics Engineers, 15th Annual Automotive Composites Conference and Exhibition, 2015.

[50] Y. Sinchuk, P. Kibleur, J. Aelterman, M. N. Boone, W. Van Paepegem, Variational and deep learning segmentation of very-low-contrast x-ray computed tomography images of carbon/epoxy woven composites, Materials 13 (2020) 936.

[51] M. W. Czabaj, M. L. Riccio, W. W. Whitacre, Numerical reconstruction of graphite/epoxy composite microstructure based on sub-micron resolution x-ray computed tomography, Composites Science and Technology 105 (2014) 174–182.

[52] P. J. Creveling, W. W. Whitacre, M. W. Czabaj, A fiber-segmentation algorithm for composites imaged using x-ray microtomography: Development and validation, Composites Part A: Applied Science and Manufacturing 126 (2019) 105606.

[53] M. J. Emerson, K. M. Jespersen, A. B. Dahl, K. Conradsen, L. P. Mikkelsen, Individual fibre segmentation from 3d x-ray computed tomography for characterising the fibre orientation in unidirectional composite materials, Composites Part A: Applied Science and Manufacturing 97 (2017) 83–92.

[54] M. J. Emerson, V. A. Dahl, K. Conradsen, L. P. Mikkelsen, A. B. Dahl, Statistical validation of individual fibre segmentation from tomograms and microscopy, Composites Science and Technology 160 (2018) 208–215.

[55] V. A. Dahl, M. J. Emerson, C. H. Trinderup, A. B. Dahl, Content-based propagation of user markings for interactive segmentation of patterned images, in: Proceedings of the IEEE/CVF Conference on Computer Vision and Pattern Recognition Workshops, 2020, pp. 994–995.

[56] K. Kamnitsas, C. Ledig, V. F. Newcombe, J. P. Simpson, A. D. Kane, D. K. Menon, D. Rueckert, B. Glocker, Efficient multi-scale 3d cnn with fully connected crf for accurate brain lesion segmentation, Medical image analysis 36 (2017) 61–78.

[57] A. Prasoon, K. Petersen, C. Igel, F. Lauze, E. Dam, M. Nielsen, Deep feature learning for knee cartilage segmentation using a triplanar convolutional neural network, in: International conference on medical image computing and computer-assisted intervention, Springer, 2013, pp. 246–253.

[58] W. Whitacre, M. Czabaj, Automated 3d digital reconstruction of fiber reinforced polymer composites, in: AIAA Guidance, Navigation, and Control Conference, 2015, p. 0342.

[59] H. Altendorf, 3D Morphological analysis and modeling of random fiber networks: applied on glass fiber reinforced composites, Ph.D. thesis, Paris, ENMP, 2011.

[60] K. Breuer, M. Stommel, Rve modelling of short fiber reinforced thermoplastics with discrete fiber orientation and fiber length distribution, SN applied Sciences 2 (2020) 1–13.

[61] L. Wang, G. Nygren, R. L. Karkkainen, Q. Yang, A multiscale approach for virtual testing of highly aligned short carbon fiber composites, Composite Structures 230 (2019) 111462.

[62] M. J. Emerson, K. M. Jespersen, Y. Wang, P. J. Withers, V. A. Dahl, K. Conradsen, L. P. Mikkelsen, A. B. Dahl, Insegt fibre: A powerful segmentation tool for quantifying fibre architecture in composites, in: Int. Conf. Tomography of Materials & Structures. Cairns, Australia, 2019.

[63] A. Nasirov, I. Fidan, Prediction of mechanical properties of fused filament fabricated structures via asymptotic homogenization, Mechanics of Materials 145 (2020) 103372.

[64] S. Wilkins, T. E. Gureyev, D. Gao, A. Pogany, A. Stevenson, Phase-contrast imaging using polychromatic hard x-rays, Nature 384 (1996) 335–338.

[65] S. Van der Walt, J. L. Schönberger, J. Nunez-Iglesias, F. Boulogne, J. D. Warner, N. Yager, E. Gouillart, T. Yu, scikit-image: image processing in python, PeerJ 2 (2014) e453.

[66] S. R. Biswal, T. Sahoo, S. Sahoo, Prediction of grain boundary of a composite microstructure using digital image processing: A comparative study, Materials Today: Proceedings 41 (2021) 357–362.

[67] P. Virtanen, R. Gommers, T. E. Oliphant, M. Haberland, T. Reddy, D. Cournapeau, E. Burovski, P. Peterson, W. Weckesser, J. Bright, S. J. van der Walt, M. Brett, J. Wilson, K. J. Millman, N. Mayorov, A. R. J. Nelson, E. Jones, R. Kern, E. Larson, C. J. Carey, İ. Polat, Y. Feng, E. W. Moore, J. VanderPlas, D. Laxalde, J. Perktold, R. Cimrman, I. Henriksen, E. A. Quintero, C. R. Harris, A. M. Archibald, A. H. Ribeiro, F. Pedregosa, P. van Mulbregt, SciPy 1.0 Contributors, SciPy 1.0: Fundamental Algorithms for Scientific Computing in Python, Nature Methods 17 (2020) 261–272.

[68] The opencv reference manual: Image segmentation with watershed algorithm, 2014. URL: https://docs.opencv.org/4.x/d3/db4/tutorial_py_watershed.html.